Environmental Science Nano

Accepted Manuscript

ROYAL SOCIETY OF CHEMISTRY

rsc.li/es-nano

NANOIMPACT STATEMENT

Functionalization of super paramagnetic iron oxide nanoparticles with different coatings renders them with unique physicochemical properties for a broad range of applications. However there is a gap between the promises of any new functionalized nanoparticle and the effects of the coatings on the nanosafety. This manuscript presents a strategy based on the integration of well-established early warning signals in an index that could reveal the relationship between the nanoparticle physico-chemical properties and their impact in the exposure. This index developed here could offer an initial rationale to choose either modifying the nanoparticle properties to reduce its nanoimpact or performing a complete risk assessment to define the risk boundaries.

Susana Cristobal and co-authors

Environmental Science Nano

RSCPublishing

ARTICLE

Cite this: DOI: 10.1039/x0xx00000x

DOI: 10.1039/x0xx00000x

www.rsc.org/

Assessment of functionalized iron oxide nanoparticles *in vitro*: introduction to integrated nanoimpact index

N. Bayat[a]‡, V.R. Lopes[b]‡, M. Sanchez-Dominguez[c], R. Lakshmanan[d], G.K. Rajarao[d] and S. Cristobal[b,e]*

Functionalization of super paramagnetic iron oxide NPs (SPIONs) with different coatings renders them with unique physicochemical properties that allow them to be used in a broad range of applications such as drug targeting and water purification. However, it is required to fill the gap between the promises of any new functionalized SPIONs and the effects of these coatings on the NPs safety. Nanotoxicology is offering diverse strategies to assess the effect of exposure to SPIONs in a case-by-case manner but an integrated nanoimpact scale has not been developed yet. We have implemented the classical integrated biological response (IBR) into an integrated nanoimpact index (INI) as an early warning scale of nano-impact based on a combination of toxicological end points such as cell proliferation, oxidative stress, apoptosis and genotoxicity. Here, the effect of SPIONs functionalized with tri-sodium citrate (TSC), polyethylenimine (PEI), aminopropyl-triethoxysilane (APTES) and Chitosan (chitosan) were assessed on human keratinocytes and endothelial cells. Our results show that endothelial cells were more sensitive to exposure than keratinocytes and the initial cell culture density modulated the toxicity. PEI-SPIONs had the strongest effects in both cell types while TSC-SPIONS were the most biocompatible. This study emphasizes not only the importance of surface coatings but also the cell type and the initial cell density on the selection of toxicity assays. The INI developed here could offer an initial rationale to choose either modifying SPIONs properties to reduce its nanoimpact or performing a complete risk assessment to define the risk boundaries.

Introduction

Super paramagnetic iron oxide NPs (SPIONs) are small synthetic γ-Fe_2O_3 (maghemite) or Fe_3O_4 particles currently of special interest due to their magnetic properties, ease of separation, recovery, and specific interaction with molecules[1]. With proper targeted surface modification, SPIONs gain additional unique characteristics such as improved biocompatibility, resistance to protein adsorption, and increase circulation time and internalization efficiency, which opened the spectra of utilization of those NPs from drug delivery, separation and purification of cells and proteins, to magnetic resonance imaging [2,3]. Moreover, another remarkable application of SPIONs in biotechnology is in water treatment industry for removal of heavy metals and organic dyes[4-8,20,9,10] SPIONs are therefore one of the most widely studied and well-characterized NPs[11-13].

Surface modification enhances the application of SPIONs, nonetheless it has now been confirmed that immediately after SPIONs enter biological fluids, proteins and other biomolecules present bind to their surface leading to the formation of a dynamic protein corona that critically defines the biological identity of the SPIONs and thereby their interaction with the cells[14]. Therefore it is important to assess whether the protein corona affects the properties of functionalized SPIONs by comprehensive characterization of their physicochemical properties, assessment of their safety and understanding the mechanism behind their potential toxicity[15,16].

In this study the potential toxicity of SPIONs functionalized with different coatings i.e. tri-sodium citrate (TSC), polyethylenimine (PEI), aminopropyl-triethoxysilane (APTES) and Chitosan (chitosan) were assessed. Chitosan, made from chitin, is a biocompatible and biodegradable linear polysaccharide with antimicrobial properties and affinity for many molecules[21]. In comparison with many other polymers, the reactive functional groups present in the chemical structure of chitosan structure (i.e. alcohol, amine and amide) act as anchors for conjugation leading to bioadhesion of a myriad of substrates such as therapeutics[21,22]. Chitosan-SPIONs have been shown to support the growth of osteoblasts[17]. Therefore the development of chitosan-coated SPIONs are of great interest especially in biomedical applications [18]. APTES ($NH_2(CH_2)_3$–$Si(OC_2H_5)_3$) is an important silane coupling agent that interacts electrostatically by its amino end with protein surface groups and covalently to the oxygen atoms of oxide NPs such as SPIONs, leading to increase protein adsorption[19,20] . It has been shown the binding of substrate DNA to the APTES linker is very

strong and that APTES has high solubility in cell membranes and it can also dissolved in both polar and nonpolar solvents[16,17,15]. APTES surface-functionalized SPIONs have been used in biological applications such as cell separation and drug targeting[21,22,23]. TSC ($Na_3C_6H_5O_7$)-coated SPIONs interact with biomolecules electrostatically; in addition, TSC has antimicrobial and anticoagulant properties due to its ability to chelating ionized calcium in blood[24,25]. Finally, PEI $(C_2H_5N)_x$ is a polycation with high ionic charge density which recently has been used as a gene therapy delivery agent. PEI has a large buffering capacity and thus it has been shown to disrupt endosomal osmolality leading to lysis[8,11]. Therefore PEI has a high efficiency as a transfection reagent since endosomal release may enhance gene delivery to the nucleus of transfected cells[26,27]. Moreover, the high density of primary amino groups of PEI renders SPIONs with good colloidal stability, biocompatibility and decrease of macrophage uptake, as well as enhancing surface modification of SPIONS with different functional groups[28] . Earlier studies from the research group have shown the application of TSC-coated SPIONs for protein purification and PEI-coated SPIONs in removal of organic carbon from sewage wastewater[29-31].

Fulfilling the promise of nanotechnology requires understanding of how the desired surface modifications affect the final attributes of the SPIONs and their interaction with biological systems. Integration of the nanotoxicological response as an index could fill the gaps between the lack of any toxicological knowledge from novel SPIONs and the requirement of a complete risk assessment. Such a tool could provide early warning signals based on multiparametrical data from well-established toxicity assays, a rational cell line selection, and experience from biomarkers approaches for environmental assessment[32]. In this investigation, an integrated nanoimpact index (INI) has been developed, based on a previously described integrated biomarker response index (IBR)[33], and adjusted for key responses to exposure to SPIONs with different coatings *in vitro* including cytotoxicity, genotoxicity and oxidative stress response.

The effects of SPIONs on human keratinocytes (HaCaT) and dermal microvascular endothelial cells (HMEC-1) have been studied here, due to their high risk of exposure to SPIONs based on their applications[34-37]. The skin is the largest organ exposed to a variety of environmental stressors and it undergoes cellular uptake of SPIONs[38]. However, SPIONs that succeed in crossing the epithelial barrier either through dermal or inhalation absorption, may access the bloodstream and directly affect the vascular endothelium or be transported to other organs, such as the liver; thus potentially these SPIONs may cause the development of diseases in such organs[36,39]. In this study, the different nanotoxicity responses after the exposure of two different cell lines to functionalized SPIONs, indicated as INI, could provide sufficient early warning signals of the possible harmful effects of exposure to novel SPIONs.

Results and discussion

The physico-chemical properties of SPIONs

The selected SPIONs were synthesized and characterized to determine their size, shape, amount of organic matter and confirmation of functional group. The chemical structures of the different surface coatings are shown in Figure 1D. Core-, TSC-, and PEI-SPIONs have been previously reported and their characterization is summarized in Table 1. The shape of core-, PEI-, APTES- and Chitosan-SPIONs were spherical while TSC-SPIONs were, quasi-spherical.

The Fourier transform infrared spectroscopy (FT-IR) analysis corresponds to Core (-OH stretching), TSC (-COO stretching) and PEI (C-N stretching; NH_2 bending) which confirms their functional groups. According to TGA studies, the content of trisodium citrate in TSC-SPIONs sample was 5.5 wt %. The PEI-SPIONs sample presented its main weight loss of 21.3 wt % between 200 and 680 °C, which was attributed to TSC + PEI[30,40-43].

APTES- and Chitosan-SPIONs were characterized to complete the set of data. Figure 1A illustrates the results from transmission electron microscopy (TEM) analysis. Figure 1A (b) and (d) shows the coating covering APTES- and Chitosan-SPIONs, respectively.

The high-resolution TEM image of chitosan sample (Figure 1A(e)) as well as the selected area electron diffraction (SAED) pattern (inset to Figure 1A(f)) demonstrates the crystallinity of the SPIONs. D-spacings of 2.52, 1.32 and 1.29 Å were observed, which may correspond either to the 311, 620, and 540 lattice planes of maghemite (γ-Fe_2O_3) or the 113, 026, and 335 lattice planes of magnetite (Fe_3O_4). Both of these possible iron oxides have a cubic spinel structure.

Organic matter content in APTES- and Chitosan-SPIONs was determined by thermogravimetric analysis as shown in Figure 1B. The APTES-SPIONs contained the highest amount of organic matter, with a weight loss of 17.24 wt%. The Chitosan-SPIONs had a total weight loss of approximately 10.05 wt%. The weight loss attributed to water (below 200ºC) was about 2 wt% for Chitosan-SPIONs and 3 wt% for APTES-SPIONs. Thus, the content of organic matter was approximately 14.24 wt% for the APTES-SPIONs and 8.05% for Chitosan-SPIONs.

FTIR analysis shown in Figure 1C confirmed the presence of Chitosan and APTES on these samples. APTES is absorbed on the magnetite NPs surfaces by Fe-O-Si bonds in the silane layer, and the band corresponding to these bonds appears at around 587 cm^{-1}, overlapping with the characteristic band corresponding to the Fe-O bonds. The strong bands between 1000 and 1150 cm^{-1} are characteristic of the stretching vibration of Si-O-Si bonds. The bands at 2922 and 2854 cm^{-1} are attributed to the alkyl chain present in all silanes, due to asymmetric CH_2 stretching. The bands at 1570 and 1630 cm^{-1} are due to the N-H stretching vibration and NH_2 bending mode of free NH_2 groups. All these signals confirm the existence of APTES on the surface of APTES-coated magnetic SPIONs. Regarding the FTIR spectrum of chitosan-SPION, characteristic peaks were identified at around 3400 cm^{-1}, which corresponds to OH and NH_2 groups. The bands at 2920 and 2852 cm^{-1} correspond to the asymmetric CH_2 stretching from chitosan backbone; the bands at 1620 and 1580 cm^{-1} are attributed to NH_2 bending. The band at 1440 cm^{-1} is due to bending of primary alcoholic group; the strong band at 1340 cm^{-1} can be attributed to C-O stretching of the primary alcoholic groups. The band at 1100 cm^{-1} is due to the absorption by the vibrational motion of the C-O-C bond. The band at 570 cm^{-1} corresponds to the characteristic absorption peak of the Fe-O bond for iron oxide NPs[44].

The additional results of the physicochemical characterization of SPIONs are summarized in Table 1. All five SPIONs had significantly larger hydrodynamic size in suspension, suggesting severe aggregation and/or agglomeration. The lack of suitable surfactants to stabilize the suspension, as well as the magnetic

properties of the SPIONs contribute to the severe aggregation and large hydrodynamic size observed. The core- and TSC-SPIONs had a negative surface charge in water suspension[42], while PEI-SPIONs had a positive surface charge which agrees well with their inherent properties[13]. The TSC- and Chitosan-SPIONs dispersed in water, qualified as stable suspensions, with a value greater than +/-30mV (Malvern), followed by core- and PEI-SPIONs. The polydispersibility (PDI) values confirmed that the SPIONs were polydispersed (PDI>0.2). The SPIONs suspended in cell culture media had negative surface charge for core and TSC-SPIONs whilst PEI-SPIONs charge was modified from positive to negative with the influence of the medium composition as in agreement with earlier studies [45].

Intrinsic and extrinsic reactive oxygen species (ROS) produced by SPIONs

Oxidative stress is an essential molecular mechanism to protect cells against environmental stressors. Measurements of the SPIONs scavenge capacity of ROS such as superoxide anion and hydrogen peroxide has been evaluated in cells exposed to metal oxide SPIONs[46,47]. The SPIONS studied here neither generated any increase in the ROS level (Figure 2A, B), nor did they increase the superoxide production at any of the conditions and cells type evaluated (Figure 2C, D). To exclude the possibility that SPIONs could produce ROS intrinsically, we also measured the ROS generation in a cell-free system (Figure 2E, F). The SPIONs did not produce significant ROS in cell culture media.

Alteration of the cellular morphology

Since subcellular localization may play an important role in NPs-induced biological effects, we examined the uptake and ultra-structural effects of the SPIONs on HaCaT and HMEC-1 cells by transmission electron microscopy (TEM) (Figure 3, 4). The TEM images from both cell lines exposed to SPIONs show that the SPIONs were taken up through active transport possibly endocytosis and/or pinocytosis (shown in boxes) and were localized inside vacuoles and phagosome-like structures scattered across the cytoplasm and especially near the nucleus. Generally the internalization was more prominent in endothelial cells, an observation which has been confirmed in a previous study [37].

Additional ultrastructure features from the endothelial TEM images provide early warning of cyto- and geno-toxicity. Any mitochondrial structural damage would lead to reduction of cellular energy supply and cytotoxicity while the alteration of the nucleus shape could indicate cyto- and geno-toxicity. SPIONs were not found in any other cytoplasmic organelles or within the nucleus. Although the SPIONS did not cause severe adverse effects on the cellular ultrastructure, some effect on the morphology of the endothelial cells nucleus was observed especially in the cells exposed to core, TSC- and PEI-coated SPIONs, which are in agreement with the genotoxicity data obtained.

In HaCaT cells exposed to SPIONS changes in nucleus morphology were not observed, however mitochondria showed swollen and elongated forms and abnormal mitochondrial cristae. With regards to the uptake of the SPIONs in the cells, protein corona, surface charge and type of surface functionalization should be taken into consideration. As described earlier, all the SPIONs in this study possessed negative surface charge in the cell culture media (Table 1), an indication of the formation and effect of the protein corona. It has been reported the positive charge of functionalized SPIONs facilitates their none-specific interaction with binding sites on the cell surface which has an average negative charge and thus enhance their uptake in cells [37,48, 49-52]. However, there are specific binding sites with cationic receptors on the cell membrane that allow interaction with and uptake of negatively charged SPIONs, i.e. through "adsorptive endocytosis" pathway [53,54,55]

In an experiment with two functionalized SPIONs with opposite surface charge, formation of protein corona resulted in a negative surface charge, irrespective of the SPION-core charge, yet nonetheless PEI-SPIONs (positively charged) were incorporated in much larger amounts than the negatively charged SPIONs[56]. In contrast in another study 15–25 nm Chitosan-SPIONs were found outside osteoblasts attached to the cell membrane[17]. In our study however the Chitosan-coated SPIONs were internalized in both cell lines possibly due to smaller size as well as type of cells.

Effect of SPIONs on cell viability

We evaluate the dose-dependent effects of SPIONs on cell viability, on both HMEC-1and HaCaT using MTT assay (Figure 5). It has been shown that the density and confluency of mammalian cell monolayers affects cytotoxicity results[57,58], therefore we performed the assay at high (1 $x10^5$ cells/ml) and low ($5x10^4$ cells/ml) cell density for both cell lines. The cell density was chosen established on the optimal density cell advised for each assay.

At the initial low cell density, HMEC-l and HaCaT cell lines displayed an opposite cellular responses. The common cellular response for HMEC-l cells was a significant decrease in cell viability (up to 70-80%) at all concentrations and SPIONs types whereas the HaCaT cells response was a significant cell proliferation. (Figure 5A, C). On the one hand, HaCaT cell proliferation response can be interpreted as activation of adhesion, growth and proliferation pathways, as shown in previous works[59]. In both cases PEI-SPIONs at 200 mg/l revealed the highest cytotoxic impact. On the other hand, at the initial high cell density of HMEC-l cell lines, SPIONs decreased significantly the cell viability in a concentration-dependent manner whereas this effect was only seen in HaCaT exposed to PEI-SPIONs. The maximal impact reaches 30% significantly decrease of cell viability for exposure to both core- and TSC-SPIONs, and up to 40% for PEI-SPIONs (Figure 5B, D). Discussing the effect of cell type on the toxicity results, the endothelial cells were more sensitive than keratinocytes for all the SPIONs. The toxicity of SPIONs to endothelial cells been shown in previous studies[60,61]. The sensitivity of endothelial cells compared to keratinocytes to NPs exposure has been confirmed by other studies[62].

Chitosan and APTES coated-SPIONs decreased cell viability in both cell types but only for both initial densities of HMEC-l cells. For HaCaT cells, only 50 or 100 mg/l concentrations induced cell viability decrease with high initial density. Chitosan-SPIONs have been shown to enhance osteoblast proliferation, decreased cell membrane damage, and promoted cell differentiation[17] while APTES-SPIONs have been reported to be biocompatible and thus suitable for drug targeting[63,64]. These finding emphasizes the importance of cell type and initial cell density on the toxicity results of SPIONs.

Multiparameter analysis of apoptosis

Apoptosis is a complex biological phenomenon with wide-range of implication in the tissue functionality. It involves diverse cellular events from the loss of cell membrane asymmetry, cell shrinkage, nuclear fragmentation, and chromatin condensation. We monitored two apoptotic events: the dissipation of the mitochondrial membrane potential and nuclear morphology. The mitochondrial membrane

potential was calculated based on the tetramethylrhodamine ethyl ester (TMRE) staining intensity. This measurement provides a sensitive parameter of the cellular oxidative balance and the NP-mediated toxicity. The nuclear morphology was evaluated by measuring the fluorescence intensity of cells treated with Hoechst dye.

The endothelial cells exposed to core-SPIONs induced significant increases of the mitochondrial membrane potential at the higher concentration whereas the exposure to the other modified SPIONs did not alter the mitochondria membrane potential (Figure 6A). The keratinocytes exposed to SPIONs, except Chitosan-, APTES- and PEI-SPIONs, led to a significant and dose-dependent increase in fluorescence intensity (Figure 6B). Chitosan-SPIONs did not affect the mitochondria membrane potential at any concentrations, in good agreement with previous findings[17].

The increased fluorescence may suggest accumulation of net negatively charged O2•-within the mitochondrial membrane. Considering that SPIONs could inhibit the electron transport chain enzymatic complexes (Complex I and III), any impairment of the mitochondrial function would affect the redox potential equilibrium and normal cellular function[65]. The loss of mitochondrial membrane integrity, opening of the permeability transition pore and subsequent ROS production are the classical toxic effect leading to cell death[66,32].

Regarding the evaluation of the nuclear morphology, the values were lower in HMEC-1 cells compared to HaCaT cells (Figure 6B, D). Nevertheless, all SPIONs showed decrease of Hoechst dye fluorescence in dose-dependent manner in endothelial cells, which is directly correlated with apoptotic cells. Though for HaCaT cells no significant values were observed. However, the nuclear morphology modifications after the exposure together with the effects on cell proliferation confirm that the endothelial cells were more sensitive to NP exposure in a concentration-dependent manner.

Summarizing, our data from cell viability indicates that the endothelial cells were more susceptible to toxicity than keratinocytes. This cellular response could neither be based on the intracellular oxidative response that is very limited in both cell lines, nor on the extrinsic ROS production that was slightly higher in in the keratinocytes media. Therefore, although oxidative stress and cell viability are classical early warning signals of cellular dysfunction, additional factors should be combined to understand the possible risks.

Genotoxicity

The genotoxicity was evaluated through the DNA damage detected in the comet assay in the two cell lines at the highest concentration. In HMEC-1 cells, all NPs caused DNA strand damage except PEI-SPIONs whereas in HaCaT cell only core-, APTES- and Chitosan-SPIONs caused significant DNA damage (Figure 7).

These results indicate that the endothelial cells are more susceptible than keratinocytes to DNA damage upon exposure. In both cell lines, core-SPIONs caused DNA stand breakage while PEI-SPIONs were non-genotoxic despite being cytotoxic. Nevertheless, the other SPIONs offered contradictory results. Our results are in agreement with previous a report of the induction of DNA damage in skin human cells exposed to SPIONs[67]. In addition, the capability of SPIONs to induce genotoxicity in the absence of cytotoxicity has been also reported [68]. The genotoxicity observed is unlikely to be mediated through ROS production.

Integrated nanoimpact index (INI)

In the previous section, a set of toxicological parameters were applied to provide early warning signals of nanoimpact at a broad range of concentrations. However, the differences in the data obtained based on the type of assays, units, and control conditions compromise its utility for inter-experimental data comparison.

Therefore, our next step was to develop an INI that could reveal the risk of exposure to any novel NPs in cells. This index has been based in the integrated biomarker response (IBR) applied in large environmental biomonitoring programme[33]. Applying a simple multivariate graphic method, the nanotoxicological data were normalized, the area inside the curve was quantified, and the nanoimpact was determined as an index.

One challenge in the development of such index was the identification of a suitable reference control among the different assays. Therefore in this study we have compared the calculated INI for each SPION as a percentage of the total effects. We arbitrarily defined the nanoimpact for this INI as: 0-10 as low impact, >10-40 as medium impact, and >40 as high impact. The starplots are shown in Figure 8 and INI values are shown in Figure 9. Endothelial cells were more sensitive to all the SPIONs which had similar medium INI values (17-26 %) with PEI-SPION and TSC-SPIONs having the highest and lowest INI value. Interestingly, in the case of keratinocytes only PEI-SPIONs had severe effects with an INI of almost 80% while the other SPIONs had similar negligible INI (all <6%). We can therefore conclude that PEI-SPIONs were the most potent SPION in both cell types and therefore further investigation is needed.

The highest challenges of applying and modifying the classical IBR to measure nanoimpact are: (1) to integrate the induction and inhibition effects with an equal value in the total impact, (2) to consider the variability and complexity of the biological response; and (3) to normalize, and correlate of the individual units per parameter and the response. Finally, the INI developed in this investigation can be applied to estimate the variations in a nanoimpact scale from any newly synthesized NPs that lack any preliminary toxicological data. Here, we demonstrated that application of the integrated biomarker concept for the interpretation of nanotoxicological responses could assist in the visualization of early warning responses and to classify the nanoimpact level in low, medium and high impact. Further decisions in the direction of performing a complete risk assessment or turning back to the synthesis and add modifications to the NP of interest can be taken at this early stage, saving time and resources.

Conclusions

Fulfilling the promises of nanotechnology requires a parallel development of nanotoxicology. The explosion of high-throughput methodologies to assist this process still requires accessibility to high-resolution analytical instruments.

In our case study, the application of INI reveal that PEI-SPIONs, with the highest INI value in both cell types, need special attention in future applications. In general, the integration of well-established early warning signals in an index could reveal the relationship between the NP physico-chemical properties of the NPs and their possible impact in the exposure. This index can be helpful in assessing the risks of exposure of any novel engineered SPIONs at an early stage of design and

synthesis and the cellular responses observed could target the future direction of NP modifications. The selection of toxicological parameters and cells presented here does not pretend to be universal but the formulation can be applied to any rational defined set of parameters.

Experimental

Synthesis and characterization of studied SPIONs. Magnetic iron oxide core SPIONs and TSC-SPIONs were prepared using co-precipitation method as mentioned earlier [42]. The techniques such as TEM, FT-IR and zeta potential were performed for core-, TSC- and PEI-SPIONs and reported elsewhere [13,26,28]. APTES was used as an amino-silane coupling agent with $–NH_2$ surface functional group on to the core. The magnetic nanoparticles suspension (150 mg) was dispersed in 100 ml of milli-Q water. APTES was added drop wise into the reaction mixture in the presence of N_2 atmosphere at 70ºC for 3 h. The prepared APTES-SPIONs were collected with an external magnetic field and washed with ethanol followed by milli-Q water. Finally, APTES-SPIONs were re-suspended in 20% ethanol and stored at 4ºC prior to use. Chitosan is a biopolymer with acetylated glucosamine and high content of $–NH_2$ groups with many advantages such as selectivity, hydrophilicity, biocompatibility and biodegradability. The SPION suspension (180 mg) was dispersed in 225 ml of deionised water. Consequently 0.68 g of chitosan was dissolved in 25 ml of acetic acid (100% glacial CH_3COOH) and added to the NP suspension. The reaction mixture was kept at room temperature for 24 h without shaking conditions. Later the chitosan-SPIONs were separated using an external magnetic field and washed with ethanol followed by milli-Q water. Finally, chitosan-SPIONs were resuspended in 20% ethanol in water and stored at 4ºC prior to use.

Thermogravimetric analysis (TGA). The TGA was carried out by heating a few mg of sample from 25 ºC to 800 ºC in a TGA-50 equipment from Shimadzu, using a heating rate of 10 ºC/min.

Zeta potential and dynamic light scattering (DLS). The measurements were performed in triplicates at 200 mg/l in sterile deionized water (with 5mM NaCl for background low ionic strength) at 25ºC, or in the complete cell media from both cell lines at 37ºC. The polydispersity index (PDI) was also assessed. The measurements were evaluated with Malvern Zetasizer Nano series V5.03 (PSS0012-16 Malvern Instruments, Worcestershire, UK) and the analysis program dispersion technology software (Malvern Instruments).

Cell culture and exposure conditions The human keratinocyte (HaCaT) and human dermal microvascular endothelial cell lines (HMEC-1) were purchased from CLS Cell Lines Service GmbH (Germany, CLS order no. 300493) and the Center for Disease Control and Prevention (CDC, Atlanta, GA, USA), respectively. The HaCat cells were cultured in Dulbecco's Modified Eagle Medium (DMEM) with high glucose and 2mM L-glutamine (without Sodium Pyruvate and HEPES; Life Technologies), and supplemented with 10% fetal bovine serum (FBS) (E.U. Approved-South American; Life Technologies) and antibiotics (penicillin 100 IU/ml, streptomycin 100 µg/ml; Life Technologies). The endothelial cells were cultured in MCDB 131 (Life technologies #10372019) and supplemented with 10% FBS (E.U. Approved-South American; Life Technologies), 10 ng/ml epidermal growth factor (mouse culture grade; BD), hydrocortisone (1 µg/ml; (Life Technologies), L-glutamine (10mM/l; Life Technologies) and antibiotics (penicillin 100 IU/ml, streptomycin 100 µg/ml; Life Technologies). The cells were maintained in a humidified atmosphere (5% CO_2) at 37°C. At 80-90% confluence, the cells were harvested using 0.05% trypsin (Life Technologies) and sub-cultured in six-well plates and 96-well plates according to the experiment being performed. The cells were allowed to attach for 24 h before the exposure. The SPIONs were suspended in cell culture medium and sonicated using a sonicator bath (1510 Branson) at room temperature for 30 min at 40 kHz and vortexed vigorously to avoid NP aggregation. The NP suspensions were diluted in medium (0, 50, 100, and 200 mg/l) and added to cells. The control samples were prepared with untreated cells were cultivated under identical conditions.

MTT assay. The *in vitro* cytotoxic effects of SPIONs were determined using standard MTT assay described *Carmichael et al* (1987) with slightly modifications[69]. The cells were seeded at different initial densities (5×10^4 and 1×10^5 cells/ ml). Briefly, cells were seeded on 96-well plates at 5×10^4 and 1×10^5 cells/ml and cultured for 24 h at 37 °C and 5% CO_2 in culture medium. The different concentrations of SPIONs were added to each well (0, 50, 100, and 200 mg/l). After incubation for 24 h, medium in each well was discarded, washed with PBS (without calcium and magnesium) and replaced with 200 µl fresh medium plus 20 µl of MTT expand (Sigma) solution filtered (5 mg/ml in PBS) was added to each well at 37°C in the dark for at least 2 h. The medium was discarded and formazan crystals were dissolved in 200 µl of dimethyl sulfoxide. Microplates were put on a shaker at 150 rpm for 10 min room temperature. The MTT reduction was quantified by absorbance at a measurement wavelength of 560 nm and a reference wavelength of 670 nm using a microplate absorbance Reader (Bio-Tek Instruments). The relative cell viability was determined as (OD treated – OD reference)/(OD control – OD reference) × 100%, where optical density (OD) treated was obtained from the cells treated with magnetic SPIONs, OD control from the untreated control cells, and OD reference from the OD of reference wavelength.

Total ROS/superoxide detection. To directly monitor real time ROS and superoxide production in live cells due to exposure to magnetic SPIONs, total ROS detection kit was used according to instructions provided by the manufacturer (Enzo Life Science). This assay distinguishes between different reactive species, such as hydrogen peroxide, peroxynitrite and hydroxyl radicals. Briefly, the cells were seeded on a black 96-well microplate at a density of ($2x10^4$ cells/ml) and incubated in a CO_2 incubator at 37ºC overnight. The cells were then treated with different concentration of magnetic SPIONs (0, 50, 100, and 200 mg/l) in triplicates and incubated for 24 h at 37ºC in a CO_2 incubator. After treatment each well solution was removed, and 100 µl of ROS/superoxide detection reagent provided in the assay was added to each well. The plate was incubated for 60 min at 37ºC. Then the plate was measured in a fluorescence reader (for total ROS) (Excitation/Emission= 488nm/520nm) and for Rhodamine (for superxide) (Excitation/Emission= 550nm/610nm).

Cell-free ROS assay. To study the oxidative potential of the magnetic SPIONs, a cell-free method with some modification was utilized [70].[70]. Briefly, 25 µl of 2′, 7′-dichlorofluoroscein diacetate (DCFH-DA) at 2.2 mM was hydrolyzed to DCFH at pH 7.0 with 100 µl of 0.01 N NaOH for each sample for 30 min in darkness. The reaction was stopped with PBS, 5 µl of horseradish peroxidase (20 U/ml) was added, incubated at 37°C for 120 min and the DCFH oxidation was measured at 485 nm/530 nm. The magnetic SPIONs were suspended in both cell culture mediums used and the concentrations analyzed were (0, 50, 100, and 200 mg/l) and 1mM H_2O_2 was used as positive controls.

Multiparameter analysis of apoptosis The *in vitro* apoptotic effect of the SPIONs was assessed with a multi-parameter apoptosis assay according to instructions of the manufacturer (Cayman Chemical Company, MI, USA). The assay employs tetramethylrhodamine ethyl ester (TMRE) as a probe for mitochondrial membrane

potential, and Hoechst Dye to evaluate the nuclear morphology. Briefly, the cells were cultured on a 96-well black culture plates at $1x10^5$ cells/ml in a CO_2 incubator at 37°C overnight. The cells were then treated with different concentrations of SPIONs suspension (0, 50, 100, and 200 µg/ml) in triplicate. After 24 h, 100 µl of TMRE/Hoecht dye staining solution was added per ml of culture medium in each well of the plate and mixed gently. The pate was then incubated in CO_2 incubator at 37°C for 30 min and the fluorescence of TMRE staining solution was measured. The cells with healthy mitochondria display strong fluorescence intensity (excitation/emission=560nm/595 nm). The fluorescence intensity of cells treated with Hoechst dye is measured at excitation/emission=355nm/465 nm.

Comet assay The DNA damage was analyzed by using alkaline comet assays according to the manufacturer's instructions (Trevigen, United Kingdom). Briefly, cells were seeded on 6-well plates at a density of 1 $x10^5$ viable cells per ml for 24 hs at 37 °C and 5% CO_2 in culture medium exposed 24 h at 200 mg/l of magnetic SPIONs. The cells were harvested and resuspended in ice cold PBS at a density of 1 $x10^5$ cells/ml. The samples were combined with low-melting-point agarose and spread onto a precoated CometSlide ™. Then, the samples were treated with alkaline unwinding solution (300 mM NaOH, 1 mM EDTA) to denature DNA and applied to electrophoresis (constant voltage of 1 V/cm) for 30min. The slides were then stained SYBR Green DNA dye and air dried before viewing with fluorescent microscopy. The comet tail moment was recorded by randomly counting about 50 cells per slide using CometScore Pro software (TriTek Corp., VA, USA). The results were averaged with at least three independent experiments.

Statistical analysis. The data are presented as the mean and standard deviation. All analyses were performed using the GraphPad Prism 6 (GraphPad Software, Inc.). The differences between samples and control were evaluated using the analysis of variance (ANOVA). $P < 0.05$ was considered to be statistically significant.

TEM analysis

High resolution transmission electron microscopy (HRTEM) was performed for analysis of particle size, morphology, and crystallinity. The sample was prepared as follows: 0.5 mg of SPIONs were dispersed in water (4 ml) and sonicated. The large agglomerates were removed with a magnet. For analysis a drop of this dispersion was deposited onto a formvar/carbon copper grid. The observation was carried out using a field emission transmission electron microscope, JEM-2200FS, 200 kV, with 0.19 nm resolution in TEM mode, 0.1 nm resolution in scanning transmission electron microscopy (STEM) mode, and spherical aberration correction in STEM mode.

For TEM imaging, cells were exposed to 200 mg/l of SPIONs after 24 h. The cell cultures were fixed in 2% glutaraldehyde in 0,1 M sodium cacodylate and 0,1 M sucrose, pH 7,4, and postfixed in 1% OsO4 in 0,15 M sodium cacodylate buffer. The cells were dehydrated and immersed in a mixture of absolute ethanol and Epon 812 (1:1), and then embedded in pure Epon 812 in the Petri dishes. The beem capsules containing polymerized Epon were placed upside down at a straight angle to the cell layer and were polymerized for 48 h at 60°C. The Epon layer with the beem capsules was removed from the Petri dish, leaving the cells on the surface of the Epon layer. The beem capsules were removed with tweezers and ultrathin sections (60 nm) were cut with a diamond knife (Diatome; Bienne, Switzerland) on a Reichert-Jung ultracut (Vienna, Austria) and collected on Formvar-coated Cu 100-mesh grids. The sections were counterstained with uranyl acetate and lead citrate and examined in a Jeol 1230 TEM (Tokyo, Japan) at 100 kV. The samples for TEM imaging were prepared at Linköping University, imaging core facility. The TEM used was TECNAI G2 Spirit Bio TWIN (FEI Company) 120 kV with a Tungsten filament.

Integrated nanoimpact index (INI). This method is based on combining all the biological responses into one general stress index termed Integrated Biomarker Response (IBR)[33]. The calculations are based on the IBR previously described method[33] with the modifications described here briefly: (1) calculation of mean (X) and standard deviation (SD) for each SPIONs response in each assay and calculation of mean value for all SPIONs responses in each assay (M), (2) standardization of data for each assay calculated as Y= (X-M)/SD, (3) using standardized data, Z was computed as Z = Y or Z = −Y, according to biological effects in case of stimulation or inhibition, respectively, (4) the minimum value for all.

SPIONs for each assay was obtained and added to Z calculating score S (S = Z + lminl) where lminl is the absolute value, (6) the values obtained were visualized using star plot in which the radial coordinate corresponds to the values, and (7) the INI value was calculated as the area of each star plot:

$Ai= ((S_i*S_{(i+1)})* \text{Sin}(2\pi/n))/2$

Where n is the number of assays in each plot.

$INI=\sum_{i=1}^{n} Ai$

In this study we have compared the calculated INI for each SPION as a percentage of the total effects plotted in a Doughnut graph. **Notes and references**

[a] Department of Biochemistry and Biophysics. Stockholm University, Stockholm, 10691 Stockholm, Sweden.

[b] Department of Clinical and Experimental Medicine, Cell Biology, Faculty of Health Science Linköping University, 581 85 Linköping, Sweden.

[c] Centro de Investigation en Materials Avanzados (CIMAV, S.C), Unidad Monterrery, 66600 Apodaca, Mexico.

[d] Royal Institute of Technology (KTH), School of Biotechnology, 10691 Stockholm, Sweden.

[e] IKERBASQUE, Basque Foundation for Science. Department of Physiology, Basque Country Medical School, 48940 Leioa, Spain.

*Correspondence Tel: +46101030881; E-mail address: Susana.Cristobal@liu.se

‡ Both authors shared the first-author position as they have equally contributed.

AcknowledgementsThis work was supported by grants from the Swedish Research Council (SC), Carl Trygger Foundation (SC), VINNOVA (SC), Oscar and Lilli Lamms Minne Foundation (SC), IKERBASQUE, Basque Foundation for science (SC), Ångpanneförening Research foundation (SC), ALF (SC) and LiU-support (SC), Erasmus Mundus Cooperation Window (EURINDIA) for the support of Doctorate scholarship (RL), NaNoTeCh and National Nanotechnology Laboratory of Mexico (MS-D). The authors would also like to acknowledge Dr A-S Höglund at the Imaging Facility at Stockholm University (IFSU) for support with microscopy, Cesar Leyva Porras (CIMAV, S.C.) for the HRTEM/STEM measurements and assistance; Alberto Toxqui Terán (CIMAV, S.C.) for TGA measurements, and Jose Bonilla-Cruz and Uriel Marquez-Lamas (CIMAV, S.C.) for FTIR measurements.

REFERENCES

1 Lehner, R., Wang, X., Marsch, S. & Hunziker, P. Intelligent nanomaterials for medicine: Carrier platforms and targeting strategies in the context of clinical application. *Nanomedicine: Nanotechnology, Biology and Medicine* **9**, 742-757, doi:http://dx.doi.org/10.1016/j.nano.2013.01.012 (2013).

2 Lu, A.-H., Salabas, E. L. & Schüth, F. Magnetic Nanoparticles: Synthesis, Protection, Functionalization, and Application. *Angewandte Chemie International Edition* **46**, 1222-1244, doi:10.1002/anie.200602866 (2007).

3 Theron, J., Walker, J. A. & Cloete, T. E. Nanotechnology and Water Treatment: Applications and Emerging Opportunities. *Critical Reviews in Microbiology* **34**, 43-69, doi:doi:10.1080/10408410701710442 (2008).

4 Zhang, Q. & Chuang, K. T. Adsorption of organic pollutants from effluents of a Kraft pulp mill on activated carbon and polymer resin. *Advances in Environmental Research* **5**, 251-258, doi:http://dx.doi.org/10.1016/S1093-0191(00)00059-9 (2001).

5 Liu, J.-f., Zhao, Z.-s. & Jiang, G.-b. Coating Fe3O4 Magnetic Nanoparticles with Humic Acid for High Efficient Removal of Heavy Metals in Water. *Environmental Science & Technology* **42**, 6949-6954, doi:10.1021/es800924c (2008).

6 Xu, P. *et al.* Use of iron oxide nanomaterials in wastewater treatment: A review. *Sci. Total Environ.* **424**, 1-10, doi:http://dx.doi.org/10.1016/j.scitotenv.2012.02.023 (2012).

7 Rocher, V., Siaugue, J.-M., Cabuil, V. & Bee, A. Removal of organic dyes by magnetic alginate beads. *Water research* **42**, 1290-1298, doi:http://dx.doi.org/10.1016/j.watres.2007.09.024 (2008).

8 Tang, S. C. N. & Lo, I. M. C. Magnetic nanoparticles: Essential factors for sustainable environmental applications. *Water research* **47**, 2613-2632, doi:http://dx.doi.org/10.1016/j.watres.2013.02.039 (2013).

9 Farrukh, A. *et al.* Design of Polymer-Brush-Grafted Magnetic Nanoparticles for Highly Efficient Water Remediation. *ACS Applied Materials & Interfaces* **5**, 3784-3793, doi:10.1021/am400427n (2013).

10 Varma, A. J., Deshpande, S. V. & Kennedy, J. F. Metal complexation by chitosan and its derivatives: a review. *Carbohydrate Polymers* **55**, 77-93, doi:http://dx.doi.org/10.1016/j.carbpol.2003.08.005 (2004).

11 Unsoy, G., Yalcin, S., Khodadust, R., Gunduz, G. & Gunduz, U. Synthesis optimization and characterization of chitosan-coated iron oxide nanoparticles produced for biomedical applications. *J Nanopart Res* **14**, 1-13, doi:10.1007/s11051-012-0964-8 (2012).

12 Ito, A., Shinkai, M., Honda, H. & Kobayashi, T. Medical application of functionalized magnetic nanoparticles. *Journal of bioscience and bioengineering* **100**, 1-11, doi:10.1263/jbb.100.1 (2005).

13 Perez, J. M. Iron oxide nanoparticles: Hidden talent. *Nat Nano* **2**, 535-536 (2007).

14 Tenzer, S. *et al.* Rapid formation of plasma protein corona critically affects nanoparticle pathophysiology. *Nat Nano* **8**, 772-781, doi:10.1038/nnano.2013.181 http://www.nature.com/nnano/journal/v8/n10/abs/nnano.2013.181.html#supplementary-information (2013).

15 Maynard, A. D., Warheit, D. B. & Philbert, M. A. The new toxicology of sophisticated materials: nanotoxicology and beyond. *Toxicological sciences : an official journal of the Society of Toxicology* **120 Suppl 1**, S109-129, doi:10.1093/toxsci/kfq372 (2011).

16 Jedlovszky-Hajdú, A., Bombelli, F. B., Monopoli, M. P., Tombácz, E. & Dawson, K. A. Surface Coatings Shape the Protein Corona of SPIONs with Relevance to Their Application in Vivo. *Langmuir* **28**, 14983-14991, doi:10.1021/la302446h (2012).

17 Shi, S. F. *et al.* Biocompatibility of chitosan-coated iron oxide nanoparticles with osteoblast cells. *Int J Nanomedicine* **7**, 5593-5602, doi:10.2147/ijn.s34348 (2012).

18 Lopez-Cruz, A., Barrera, C., Calero-DdelC, V. L. & Rinaldi, C. Water dispersible iron oxide nanoparticles coated with covalently linked chitosan. *Journal of Materials Chemistry* **19**, 6870-6876, doi:10.1039/B908777J (2009).

19 Can, K., Ozmen, M. & Ersoz, M. Immobilization of albumin on aminosilane modified superparamagnetic magnetite nanoparticles and its characterization. *Colloids and Surfaces B: Biointerfaces* **71**, 154-159, doi:http://dx.doi.org/10.1016/j.colsurfb.2009.01.021 (2009).

20 Liu, T., Wang, S. & Chen, G. Immobilization of trypsin on silica-coated fiberglass core in microchip for highly efficient proteolysis. *Talanta* **77**, 1767-1773, doi:10.1016/j.talanta.2008.10.009 (2009).

21 del Pozo-Rodriguez, A. *et al.* A proline-rich peptide improves cell transfection of solid lipid nanoparticle-based non-viral vectors. *Journal of controlled release : official journal of the Controlled Release Society* **133**, 52-59, doi:10.1016/j.jconrel.2008.09.004 (2009).

22 Sweetman, M. J., Shearer, C. J., Shapter, J. G. & Voelcker, N. H. Dual silane surface functionalization for the selective attachment of human neuronal cells to porous silicon. *Langmuir* **27**, 9497-9503, doi:10.1021/la201760w (2011).

23 Neuberger, T., Schöpf, B., Hofmann, H., Hofmann, M. & von Rechenberg, B. Superparamagnetic nanoparticles for biomedical applications: possibilities and limitations of a new drug delivery system. *Journal of Magnetism and Magnetic Materials* **293**, 483-496, doi:http://dx.doi.org/10.1016/j.jmmm.2005.01.064 (2005).

24 Weijmer, M. C., Debets-Ossenkopp, Y. J., Van De Vondervoort, F. J. & ter Wee, P. M. Superior antimicrobial activity of trisodium

citrate over heparin for catheter locking. *Nephrology, dialysis, transplantation : official publication of the European Dialysis and Transplant Association - European Renal Association* **17**, 2189-2195 (2002).

25 Ashouri, O. S. Regional sodium citrate anticoagulation in patients with active bleeding undergoing hemodialysis. *Renal Failure* **9**, 45-51, doi:doi:10.3109/08860228509104839 (1985).

26 Wiseman, J. W., Goddard, C. A., McLelland, D. & Colledge, W. H. A comparison of linear and branched polyethylenimine (PEI) with DCChol//DOPE liposomes for gene delivery to epithelial cells *in vitro* and *in vivo*. *Gene Ther* **10**, 1654-1662 (0000).

27 Boussif, O. *et al.* A versatile vector for gene and oligonucleotide transfer into cells in culture and in vivo: polyethylenimine. *Proceedings of the National Academy of Sciences of the United States of America* **92**, 7297-7301 (1995).

28 Li, J. *et al.* Polyethyleneimine-mediated synthesis of folic acid-targeted iron oxide nanoparticles for in vivo tumor MR imaging. *Biomaterials* **34**, 8382-8392, doi:http://dx.doi.org/10.1016/j.biomaterials.2013.07.070 (2013).

29 Huang, Y. & Keller, A. A. Magnetic Nanoparticle Adsorbents for Emerging Organic Contaminants. *ACS Sustainable Chemistry & Engineering* **1**, 731-736, doi:10.1021/sc400047q (2013).

30 Okoli, C., Boutonnet, M., Mariey, L., Järås, S. & Rajarao, G. Application of magnetic iron oxide nanoparticles prepared from microemulsions for protein purification. *Journal of Chemical Technology & Biotechnology* **86**, 1386-1393, doi:10.1002/jctb.2704 (2011).

31 Okoli, C., Boutonnet, M., Järås, S. & Rajarao-Kuttuva, G. Protein-functionalized magnetic iron oxide nanoparticles: time efficient potential-water treatment. *J Nanopart Res* **14**, 1-9, doi:10.1007/s11051-012-1194-9 (2012).

32 Sanchez, W., Burgeot, T. & Porcher, J. M. A novel "Integrated Biomarker Response" calculation based on reference deviation concept. *Environmental science and pollution research international* **20**, 2721-2725, doi:10.1007/s11356-012-1359-1 (2013).

33 Beliaeff, B. & Burgeot, T. Integrated biomarker response: a useful tool for ecological risk assessment. *Environ Toxicol Chem* **21**, 1316-1322 (2002).

34 Murray, A. R. *et al.* Oxidative stress and dermal toxicity of iron oxide nanoparticles in vitro. *Cell biochemistry and biophysics* **67**, 461-476, doi:10.1007/s12013-012-9367-9 (2013).

35 Schneider, M., Stracke, F., Hansen, S. & Schaefer, U. F. Nanoparticles and their interactions with the dermal barrier. *Dermato-Endocrinology* **1**, 197-206 (2009).

36 Luthra, S. *et al.* Evaluation of in Vitro Effects of Bevacizumab (Avastin) on Retinal Pigment Epithelial, Neurosensory Retinal, and Microvascular Endothelial Cells. *RETINA* **26**, 512-518 510.1097/1001.iae.0000222547.0000235820.0000222552 (2006).

37 Osaka, T., Nakanishi, T., Shanmugam, S., Takahama, S. & Zhang, H. Effect of surface charge of magnetite nanoparticles on their internalization into breast cancer and umbilical vein endothelial cells. *Colloids and Surfaces B: Biointerfaces* **71**, 325-330, doi:http://dx.doi.org/10.1016/j.colsurfb.2009.03.004 (2009).

38 Zhang, L. W. & Monteiro-Riviere, N. A. Use of confocal microscopy for nanoparticle drug delivery through skin. *BIOMEDO* **18**, 061214-061214, doi:10.1117/1.JBO.18.6.061214 (2012).

39 Donaldson, K., Borm, P., Castranova, V. & Gulumian, M. The limits of testing particle-mediated oxidative stress in vitro in predicting diverse pathologies; relevance for testing of nanoparticles. *Particle and fibre toxicology* **6**, 13 (2009).

40 Lakshmanan, R., Okoli, C., Boutonnet, M., Järås, S. & Rajarao, G. K. Effect of magnetic iron oxide nanoparticles in surface water treatment: Trace minerals and microbes. *Bioresource Technology* **129**, 612-615, doi:http://dx.doi.org/10.1016/j.biortech.2012.12.138 (2013).

41 Laurent, J., Jaziri, K., Guignard, R., Casellas, M. & Dagot, C. Comprehensive insight of the performances of excess sludge reduction by 90 °C thermal treatment coupled with activated sludge at pilot scale: COD and N removal, bacterial populations, fate of heavy metals. *Process Biochemistry* **46**, 1808-1816, doi:http://dx.doi.org/10.1016/j.procbio.2011.06.007 (2011).

42 Okoli, C. *et al.* Characterization of superparamagnetic iron oxide nanoparticles and its application in protein purification. *J Nanosci Nanotechnol* **11**, 10201-10206 (2011).

43 Lakshmanan, R., Sanchez-Dominguez, M., Matutes-Aquino, J. A., Wennmalm, S. & Kuttuva Rajarao, G. Removal of total organic carbon from sewage wastewater using poly(ethylenimine)-functionalized magnetic nanoparticles. *Langmuir : the ACS journal of surfaces and colloids* **30**, 1036-1044, doi:10.1021/la404076n (2014).

44 Yang, C. H. *et al.* Facile synthesis of radial-like macroporous superparamagnetic chitosan spheres with in-situ co-precipitation and gelation of ferro-gels. *PLoS One* **7**, e49329, doi:10.1371/journal.pone.0049329 (2012).

45 Steitz, B. *et al.* Characterization of PEI-coated superparamagnetic iron oxide nanoparticles for transfection: Size distribution, colloidal properties and DNA interaction. *Journal of Magnetism and Magnetic Materials* **311**, 300-305, doi:http://dx.doi.org/10.1016/j.jmmm.2006.10.1194 (2007).

46 Huang, C.-C., Aronstam, R. S., Chen, D.-R. & Huang, Y.-W. Oxidative stress, calcium homeostasis, and altered gene expression in human lung epithelial cells exposed to ZnO nanoparticles. *Toxicology in Vitro* **24**, 45-55, doi:http://dx.doi.org/10.1016/j.tiv.2009.09.007 (2010).

47 Bayat, N., Rajapakse, K., Marinsek-Logar, R., Drobne, D. & Cristobal, S. The effects of engineered nanoparticles on the cellular structure and growth of Saccharomyces cerevisiae. *Nanotoxicology* **8**, 363-373, doi:doi:10.3109/17435390.2013.788748 (2014).

48 Yue, Z.-G. *et al.* Surface Charge Affects Cellular Uptake and Intracellular Trafficking of Chitosan-Based Nanoparticles. *Biomacromolecules* **12**, 2440-2446, doi:10.1021/bm101482r (2011).

49 Kralj, S. *et al.* Effect of surface charge on the cellular uptake of fluorescent magnetic nanoparticles. *J Nanopart Res* **14**, 1-14, doi:10.1007/s11051-012-1151-7 (2012).

50 Jo, J., Aoki, I. & Tabata, Y. Design of iron oxide nanoparticles with different sizes and surface charges for simple and efficient labeling of mesenchymal stem cells. *Journal of controlled release : official journal of the Controlled Release Society* **142**, 465-473, doi:10.1016/j.jconrel.2009.11.014 (2010).

51 Influence of iron oxide nanoparticles on bending elasticity and bilayer fluidity of phosphotidylcholine liposomal membranes. *Colloids and Surfaces A: Physicochemical and Engineering Aspects* (2014).

52 Schweiger, C. *et al.* Quantification of the internalization patterns of superparamagnetic iron oxide nanoparticles with opposite charge. *Journal of Nanobiotechnology* **10**, 28 (2012).

53 Kalambur, V. S., Longmire, E. K. & Bischof, J. C. Cellular level loading and heating of superparamagnetic iron oxide nanoparticles. *Langmuir* **23**, 12329-12336, doi:10.1021/la701100r (2007).

54 Wilhelm, C., Gazeau, F., Roger, J., Pons, J. N. & Bacri, J. C. Interaction of Anionic Superparamagnetic Nanoparticles with Cells: Kinetic Analyses of Membrane Adsorption and Subsequent Internalization. *Langmuir* **18**, 8148-8155, doi:10.1021/la0257337 (2002).

55 Luciani, N., Gazeau, F. & Wilhelm, C. Reactivity of the monocyte/macrophage system to superparamagnetic anionic nanoparticles. *Journal of Materials Chemistry* **19**, 6373-6380, doi:10.1039/B903306H (2009).

56 Calatayud, M. P. *et al.* The effect of surface charge of functionalized Fe3O4 nanoparticles on protein adsorption and cell uptake. *Biomaterials* **35**, 6389-6399, doi:http://dx.doi.org/10.1016/j.biomaterials.2014.04.009 (2014).

57 Heng, B. C. *et al.* Cytotoxicity of zinc oxide (ZnO) nanoparticles is influenced by cell density and culture format. *Archives of toxicology* **85**, 695-704, doi:10.1007/s00204-010-0608-7 (2011).

58 Wataha, J. C., Hanks, C. T. & Craig, R. G. The effect of cell monolayer density on the cytotoxicity of metal ions which are released from dental alloys. *Dental materials : official publication of the Academy of Dental Materials* **9**, 172-176 (1993).

59 Hussien, R. *et al.* Unique growth pattern of human mammary epithelial cells induced by polymeric nanoparticles. *Physiological reports* **1**, e00027, doi:10.1002/phy2.27 (2013).

60 Yang, J. X., Tang, W. L. & Wang, X. X. Superparamagnetic iron oxide nanoparticles may affect endothelial progenitor cell migration ability and adhesion capacity. *Cytotherapy* **12**, 251-259, doi:10.3109/14653240903446910 (2010).

61 Wu, X., Tan, Y., Mao, H. & Zhang, M. Toxic effects of iron oxide nanoparticles on human umbilical vein endothelial cells. *Int. J. Nanomedicine* **5**, 385-399 (2010).

62 Rooney, A. D. *et al. In Vitro Toxicity of Nanoparticles in Mouse Keratinocytes and Endothelial Cells*, <http://handle.dtic.mil/100.2/ADA458356> (2004).

63 Cao, H., He, J., Deng, L. & Gao, X. Fabrication of cyclodextrin-functionalized superparamagnetic Fe3O4/amino-silane core–shell nanoparticles via layer-by-layer method. *Applied Surface Science* **255**, 7974-7980, doi:http://dx.doi.org/10.1016/j.apsusc.2009.04.199 (2009).

64 Mashhadizadeh, M. H. & Amoli-Diva, M. Drug-Carrying Amino Silane Coated Magnetic Nanoparticles as Potential Vehicles for Delivery of Antibiotics *Journal of Nanomedicine and Nanotechnology 2012, 3:4* **3** (2012).

65 Kowaltowski, A. J., de Souza-Pinto, N. C., Castilho, R. F. & Vercesi, A. E. Mitochondria and reactive oxygen species. *Free Radical Biology and Medicine* **47**, 333-343, doi:http://dx.doi.org/10.1016/j.freeradbiomed.2009.05.004 (2009).

66 Li, X. *et al.* Targeting mitochondrial reactive oxygen species as novel therapy for inflammatory diseases and cancers. *Journal of Hematology & Oncology* **6**, 19 (2013).

67 Ahamed, M. *et al.* Iron oxide nanoparticle-induced oxidative stress and genotoxicity in human skin epithelial and lung epithelial cell lines. *Current pharmaceutical design* **19**, 6681-6690 (2013).

68 Singh, N. *et al.* The role of iron redox state in the genotoxicity of ultrafine superparamagnetic iron oxide nanoparticles. *Biomaterials* **33**, 163-170, doi:http://dx.doi.org/10.1016/j.biomaterials.2011.09.087 (2012).

69 Carmichael, J., DeGraff, W. G., Gazdar, A. F., Minna, J. D. & Mitchell, J. B. Evaluation of a tetrazolium-based semiautomated colorimetric assay: assessment of radiosensitivity. *Cancer research* **47**, 943-946 (1987).

70 Foucaud, L. W., M. R.Brown, D. M.Stone, V. Measurement of reactive species production by nanoparticles prepared in biologically relevant media. *Toxicology letters* **174**, 1-9, doi:10.1016/j.toxlet.2007.08.001 (2007).

TABLE1

SPIONs	hydrodynamic size (nm)			Zeta potential			PDI		
	H_2O	HMEC-1 medium	HaCaT medium	H_2O	HMEC-1 medium	HaCaT medium	H_2O	HMEC-1 medium	HaCaT medium
Fe3O4 (core)-	5845 ±873.9	8858± 934.7	9913 ±698.9	-27.1± 1.16	-8.25± 1.30	-7.68± 1.01	0.98 ±0.03	0.68± 0.26	0.66 ±0.17
TSC-	810.4 ±42.25	1370 ±43.02	1217 ±66.69	-32.1± 1.7	-8.46± 0.71	-7.4± 0.90	0.51 ±0.04	0.55 ±0.21	0.81 ±0.09
PEI-	3459 ±157.6	5255 ±212.5	4081 ±464.1	21.8± 0.20	-3.9± 1.16	-4.45± 0.51	0.64 ±0.06	0.25 ±0.13	0.86 ±0.22
APTES-	5338 ±189.3	5675 ±1074	4882 ±455.9	4.37± 0.46	-8.33± 0.79	-9.76± 0.61	1.0 ±0.0	0.63 ±0.18	0.72 ±0.48
Chitosan-	1223 ±71.00	2553 ±148.0	1597 ±897.7	40.5± 0.53	-5.37± 0.86	-9.57± 1.50	0.58 ±0.00	0.47 ±0.063	0.59 ±0.3

Table and Figure legends

Table 1. Characterization of SPIONs. SPIONs dissolved in sterile deionized water with 5 mM NaCl (at 25^{o}C), and in cell culture media of each cell lines (at 37^{o}C). PDI- Poly dispersity index.

Figure 1. (A) STEM images of: (a), (b) APTES-SPIONs and (c) chitosan-SPIONs; HRTEM images of (d), (e), (f) APTES-SPIONs. SAED pattern of image (f) shown as inset, (B) TGA and (C) FTIR of chitosan- and APTES-SPIONs (D) The chemical structure of different coatings of SPIONs

Figure 2. Oxidative stress production. Total intracellular ROS levels in HMEC-1 (A) and HaCaT (B) cells upon exposure to SPIONs for 24h. Total intracellular superoxide levels in HEMC-1 (C) and HaCaT (D) cells after 24h exposure. Cell-free DCFH (ROS) assay of SPIONs in HMEC-1 cell culture (E) and HaCaT (F) cell culture ,emdia after 120 min. The SPIONs concentrations in all experiments were 0, 50, 100 and 200mg/l. * p<0,05, *** p<0,001, and**** p<0,0001. Three biological and three technical replicates for each assay was performed.

Figure 3. **TEM images of keratinocytes (HaCaT) cells before and after SPIONs exposure**. The exposure concentration was 200mg/l for 24 h. Arrows indicate SPIONs localized inside vesicles across the cytoplasm. Boxes indicate the active uptake of SPIONs. Control- cells without exposure.

Figure 4. **TEM images of endothelial cells (HMEC-1) before and after SPIONs exposure**. The exposure concentration was 200mg/l for 24 h. Arrows indicate SPIONs localized inside vesicles across the cytoplasm. Boxes indicate the active uptake of SPIONs. Control- cells without exposure.

Figure 5. MTT assay. Percentage of cell viability relative to negative control of HMEC-1 and HaCaT cells after 24h-exposure to core-, TSC-, PEI-, APTES- and chitosan- SPIONs at a concentration of 0, 50, 100 and 200mg/l. Two initial cell densities wereused: HMEC-1 $5x10^4$ (A) and 1 $x10^5$ cells/ml (B) cells/ml. HaCaT cells at $5x10^4$ (C) and 1 $x10^5$ cells/ml (D) cells/ml. **** p<0,0001 and * p<0,05. Three biological and three technical replicates for each assay was performed.

Figure 6. Apoptosis events. Quantification of mitochondrial membrane potential by TMRE assay in HMEC-1 cells (A) and HaCaT (B) cells upon exposure to core-, TSC-, PEI-, APTES- and chitosan- SPIONs at a concentration of 0-200mg/l. Quantification of nuclear morphology by Hoechst dye assay in HMEC-1 (C) and HaCaT cells (D) upon exposure to core-, TSC-, PEI-, APTES- and chitosan- SPIONs at a concentration of 0-200mg/l. **** p<0,0001 and *** p<0,001 ** P<0,01 and *p<0,05. Three biological and three technical replicates for each assay was performed.

Figure 7. Genotoxicity. DNA damage was analyzed by Comet assay of HMEC-1 cells and HaCaT cells exposed to SPIONs at 200 mg/l for 24 h. **** p<0,0001 and * p<0,05. Three biological and two technical replicates for each assay was performed.

Figure 8. Star plots summarizing the cellular responses of to HMEC-1 (blue) and HaCaT cells (red) to core- (A), TSC- (B), Chitosan (C), PEI-(D), and APTES-(E) SPIONs. The abbreviations corresponds: APOP (M) - apoptosis assay, mitochondrial membrane potential, APOP (N) - apoptosis assay, nuclear morphology; ROS - intracellular reactive oxygen species; SOX - intracellular superoxide; GTOX - genotoxicity, comet assay; Prolif - cell proliferation with high (H) and low (L) seeding cell density.

Figure 9. INI values. The INI values calculated based on the star plots (figure 8) and presented as relative contribution of each SPIONs to overall impact of core-, TSC-, PEI-, APTES- and Chitosan- SPIONs in both keratinocytes (HaCaT) (A) and endothelial cells (HMEC-1) (B).

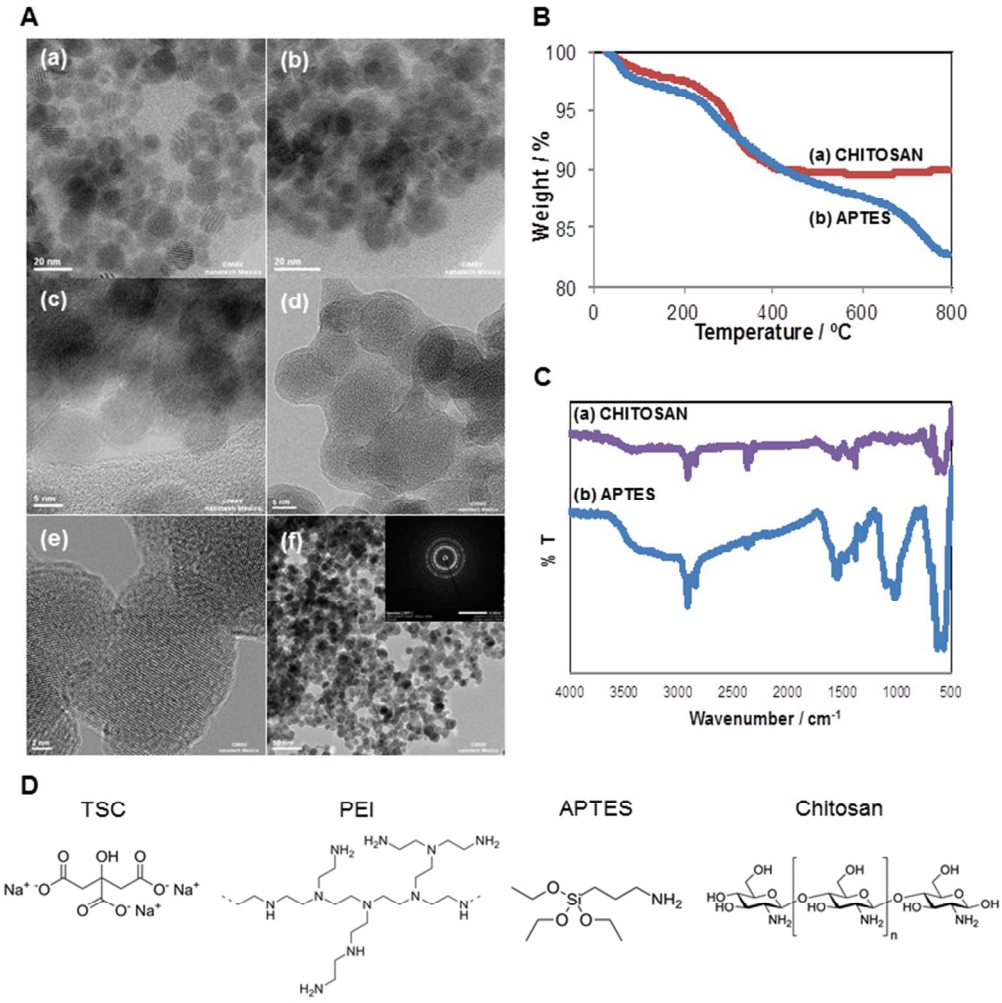

Figure 1. (A) STEM images of: (a), (b) APTES-SPIONs and (c) chitosan-SPIONs; HRTEM images of (d), (e), (f) APTES-SPIONs. SAED pattern of image (f) shown as inset, (B) TGA and (C) FTIR of chitosan- and APTES-SPIONs (D) The chemical structure of different coatings of SPIONs.
212x214mm (96 x 96 DPI)

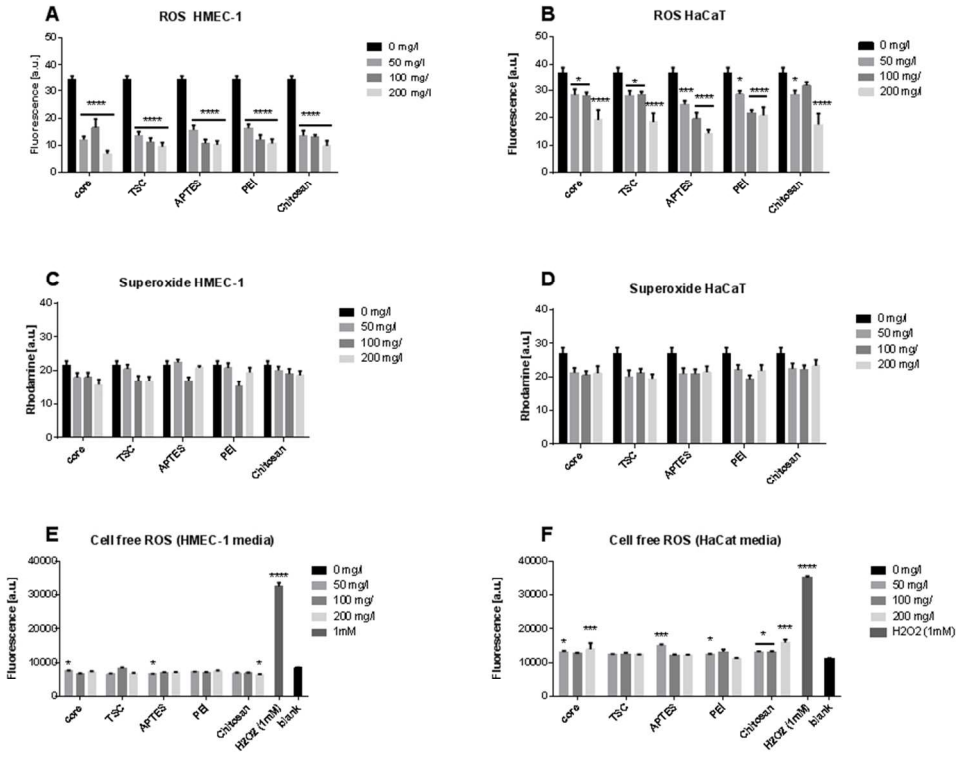

Figure 2. Oxidative stress production. Total intracellular ROS levels in HMEC-1 (A) and HaCaT (B) cells upon exposure to SPIONs for 24h. Total intracellular superoxide levels in HEMC-1 (C) and HaCaT (D) cells after 24h exposure. Cell-free DCFH (ROS) assay of SPIONs in HMEC-1 cell culture (E) and HaCaT (F) cell culture ,emdia after 120 min. The SPIONs concentrations in all experiments were 0, 50, 100 and 200mg/l. * p<0,05, *** p<0,001, and**** p<0,0001. Three biological and three technical replicates for each assay was performed.
249x197mm (96 x 96 DPI)

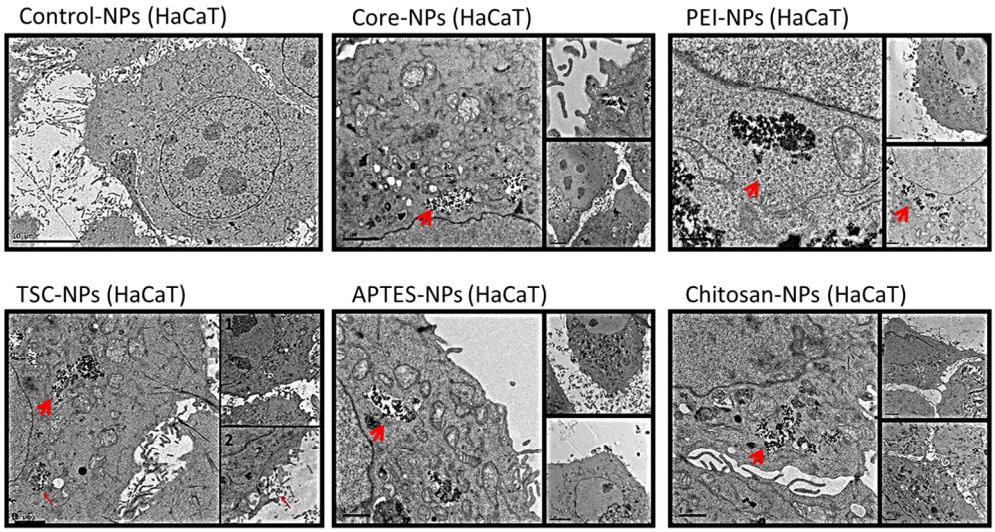

Figure 3. TEM images of keratinocytes (HaCaT) cells before and after SPIONs exposure. The exposure concentration was 200mg/l for 24 h. Arrows indicate SPIONs localized inside vesicles across the cytoplasm. Boxes indicate the active uptake of SPIONs. Control- cells without exposure.
378x205mm (96 x 96 DPI)

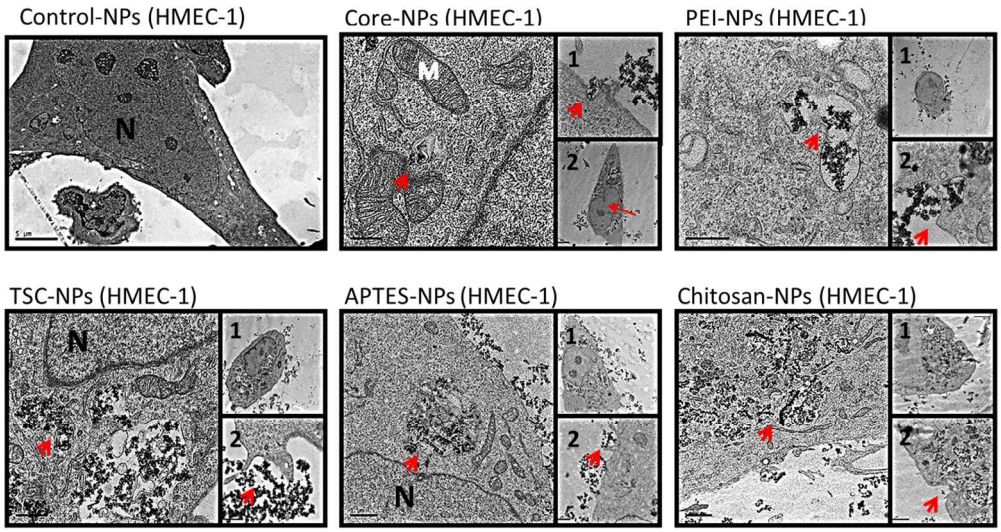

Figure 4. TEM images of endothelial cells (HMEC-1) before and after SPIONs exposure. The exposure concentration was 200mg/l for 24 h. Arrows indicate SPIONs localized inside vesicles across the cytoplasm. Boxes indicate the active uptake of SPIONs. Control- cells without exposure.
379x202mm (96 x 96 DPI)

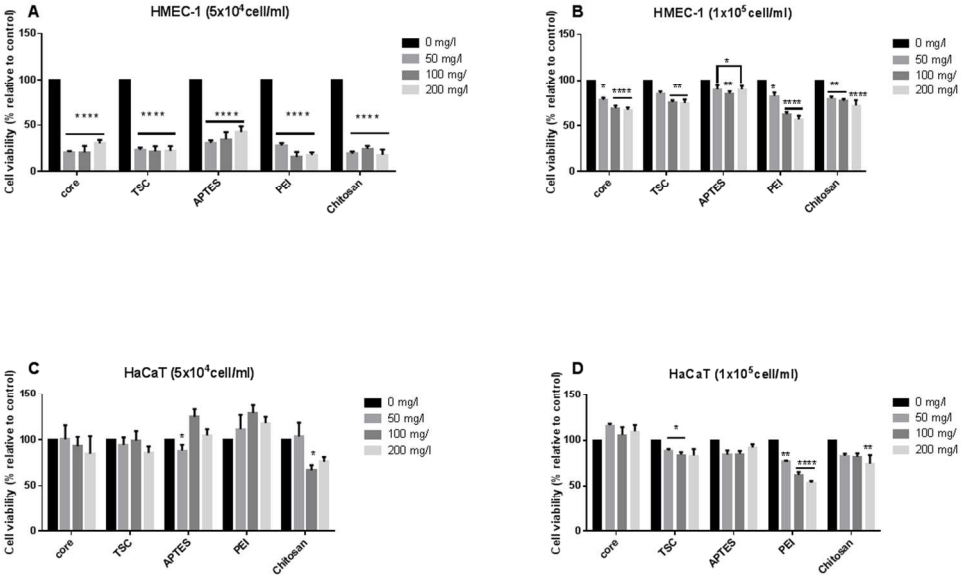

Figure 5. MTT assay. Percentage of cell viability relative to negative control of HMEC-1 and HaCaT cells after 24h-exposure to core-, TSC-, PEI-, APTES- and chitosan- SPIONs at a concentration of 0, 50, 100 and 200mg/l. Two initial cell densities wereused: HMEC-1 5x104 (A) and 1 x105 cells/ml (B) cells/ml. HaCaT cells at 5x104 (C) and 1 x105 cells/ml (D) cells/ml. **** p<0,0001 and * p<0,05. Three biological and three technical replicates for each assay was performed.
308x191mm (96 x 96 DPI)

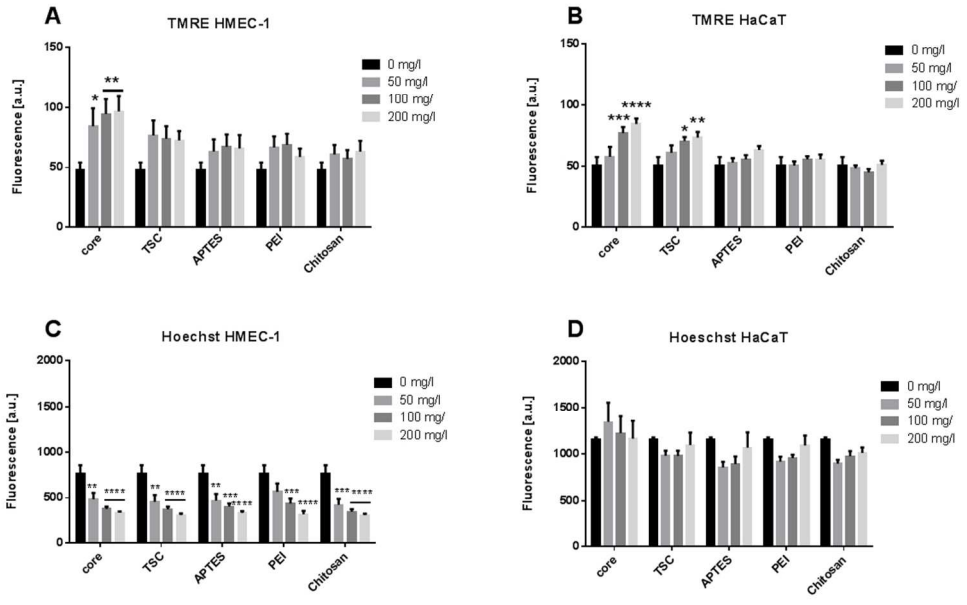

Figure 6. Apoptosis events. Quantification of mitochondrial membrane potential by TMRE assay in HMEC-1 cells (A) and HaCaT (B) cells upon exposure to core-, TSC-, PEI-, APTES- and chitosan- SPIONs at a concentration of 0-200mg/l. Quantification of nuclear morphology by Hoechst dye assay in HMEC-1 (C) and HaCaT cells (D) upon exposure to core-, TSC-, PEI-, APTES- and chitosan- SPIONs at a concentration of 0-200mg/l. **** p<0,0001 and *** p<0,001 ** P<0,01 and *p<0,05. Three biological and three technical replicates for each assay was performed.
310x196mm (96 x 96 DPI)

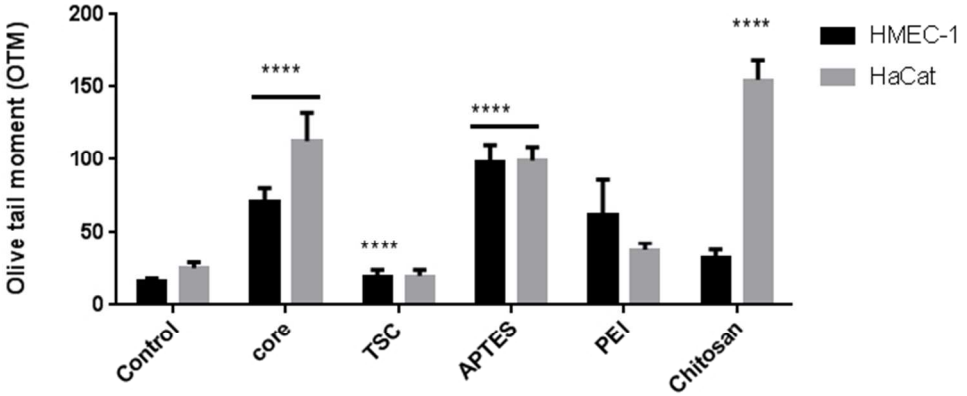

Figure 7. Genotoxicity. DNA damage was analyzed by Comet assay of HMEC-1 cells and HaCaT cells exposed to SPIONs at 200 mg/l for 24 h. **** p<0,0001 and * p<0,05. Three biological and two technical replicates for each assay was performed.
181x81mm (96 x 96 DPI)

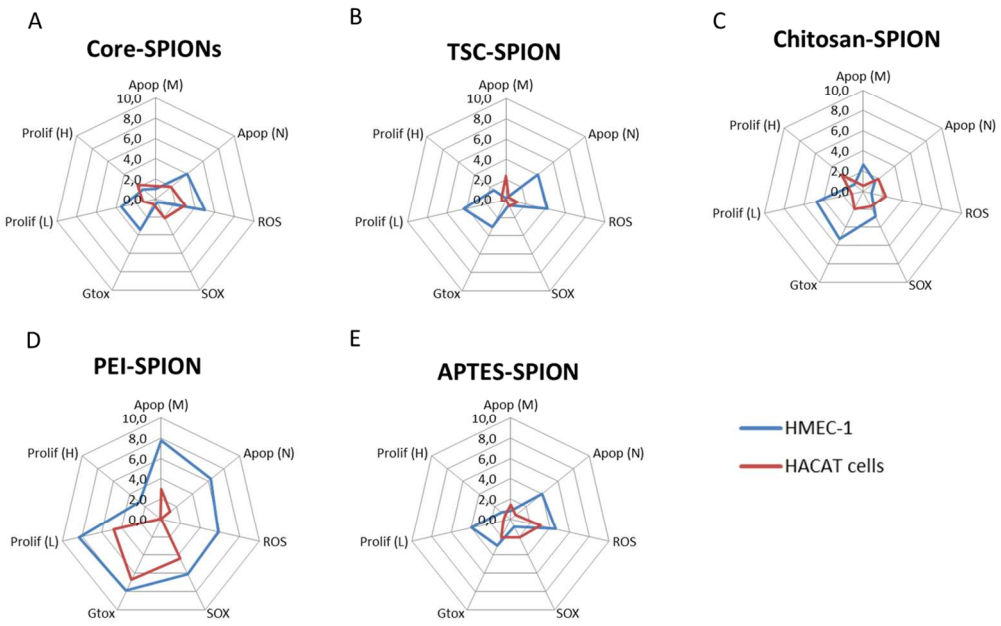

Figure 8. Star plots summarizing the cellular responses of to HMEC-1 (blue) and HaCaT cells (red) to core- (A), TSC- (B), Chitosan (C), PEI-(D), and APTES-(E) SPIONs. The abbreviations corresponds: APOP (M) - apoptosis assay, mitochondrial membrane potential, APOP (N) - apoptosis assay, nuclear morphology; ROS - intracellular reactive oxygen species; SOX - intracellular superoxide; GTOX - genotoxicity, comet assay; Prolif - cell proliferation with high (H) and low (L) seeding cell density.
374x239mm (96 x 96 DPI)

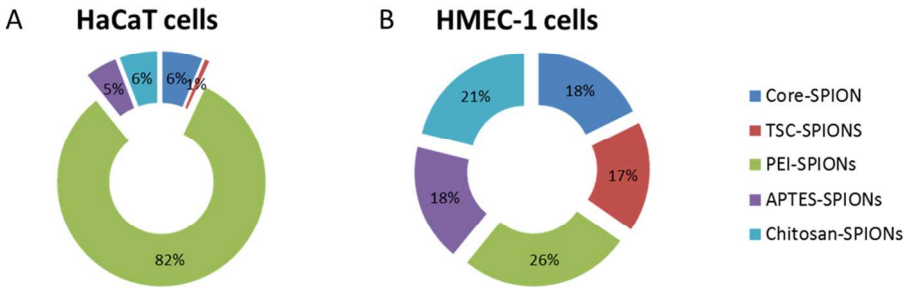

Figure 9. INI values. The INI values calculated based on the star plots (figure 8) and presented as relative contribution of each SPIONs to overall impact of core-, TSC-, PEI-, APTES- and Chitosan- SPIONs in both keratinocytes (HaCaT) (A) and endothelial cells (HMEC-1) (B).
314x107mm (96 x 96 DPI)